nature photonics

LETTERS

https://doi.org/10.1038/s41566-022-01018-7

Check for updates

Asymmetric parametric generation of images with nonlinear dielectric metasurfaces

Sergey S. Kruk[1,2,7]✉, Lei Wang[2,3,4,7]✉, Basudeb Sain[1], Zhaogang Dong[5], Joel Yang[5,6], Thomas Zentgraf[1] and Yuri Kivshar[2]✉

Subwavelength dielectric resonators assembled into metasurfaces have become a versatile tool for miniaturizing optical components approaching the nanoscale[1–3]. An important class of metasurface functionalities is associated with asymmetry in both the generation and transmission of light with respect to reversals of the positions of emitters and receivers[4–6]. The nonlinear light–matter interaction in metasurfaces[7–9] offers a promising pathway towards miniaturization of the asymmetric control of light. Here we demonstrate asymmetric parametric generation of light in nonlinear metasurfaces. We assemble dissimilar nonlinear dielectric resonators into translucent metasurfaces that produce images in the visible spectral range on being illuminated by infrared radiation. By design, the metasurfaces produce different and completely independent images for the reversed direction of illumination, that is, when the positions of the infrared emitter and the visible light receiver are exchanged. Nonlinearity-enabled asymmetric control of light by subwavelength resonators paves the way towards novel nanophotonic components via dense integration of large quantities of nonlinear resonators into compact metasurface designs.

The nonlinear optical regime describing interactions of metasurfaces with strong optical fields allows novel functionalities of metasurfaces to be acquired beyond those of their linear counterparts[7–9]. Recent examples include imaging through nonlinear meta-lenses[10], nonlinear topological transitions[11], bistability[12] and optical pulse shaping[13]. The efficiency of nonlinear processes in subwavelength photonics can be increased by using high-index dielectric nanoparticles supporting multipolar Mie resonances and composite modes[14]. An important cluster of functionalities enabled by nonlinear light–matter interactions is associated with the asymmetric control of light[4–6,15,16].

Traditionally, the asymmetric control of light is realized with bulky optical components[4–6]. Relatively more compact photonic chips have been demonstrated using coupled-waveguide micro-resonators[15], and a plasmonic nonlinear metasurface with asymmetries in its optical response has been demonstrated experimentally[16]. The metasurface functionality has relied on a geometric phase gradient created over a distance of several wavelengths. Accordingly, the approaches experimentally demonstrated so far have relied on building blocks that were substantially larger than the wavelength of light in at least one spatial dimension. This has hindered the dense integration of large quantities of such photonic components into compact systems analogous to the integration of large quantities of electronic components into semiconductor chips. Recently, there has been interest in theoretical investigations of various nonlinear photonics platforms for asymmetric light control at the subwavelength scale[17–22]. An earlier theoretical concept of asymmetric nonlinear control of electromagnetic waves with metaphotonics was proposed in ref. [17]. The authors presented a nonlinear structure acting as a Faraday rotator without an external magnetic field. For this design, they employed a combination of chiral metasurface elements with strongly nonlinear metasurface elements integrated into a Fabry–Pérot cavity. To achieve a strong nonlinear response, the authors proposed to implement varactor diodes into the design, which made that concept immediately applicable in the microwave frequency range but imposed challenges for its realization in optics. As of today, none of the existing theoretical proposals for nonlinear asymmetric control of light[17–22] have been realized experimentally.

In this Letter we develop theoretically and demonstrate experimentally all-dielectric metasurfaces producing a nonlinear asymmetric generation of light. When infrared light passes through the metasurfaces, certain encoded images are observed, as sketched in Fig. 1. However, once we flip the metasurfaces to the opposite side, we observe completely different images.

The functionality of the developed resonators relies on an interplay between nonlinear light–matter interactions and magneto-electric coupling[23,24] to its artificially engineered optical modes. Magneto-electric coupling has facilitated many peculiar photonic functionalities both in microwaves and optics, including polarization transformations[25,26], anomalous transmission[27,28] and reflection[29,30], photonic analogues of spin-Hall effects[31], photonic Jackiw–Rebbi states[32] and nontrivial topological phases[33].

We first study metasurfaces made of identical asymmetric nonlinear resonators. The resonators are nanocylinders whose optical response at the fundamental wavelength is dominated by two Mie multipoles: the electric dipole (ED) and the magnetic dipole (MD), with smaller contributions from higher-order multipoles. The nanocylinders consist of two layers of materials with different optical constants: amorphous silicon and silicon nitride (Fig. 2a,b). Silicon, in comparison to silicon nitride, has a higher refractive index and higher nonlinear susceptibility. In our geometry, the magneto-electric coupling arises from the asymmetry introduced

[1]Department of Physics, Paderborn University, Paderborn, Germany. [2]Nonlinear Physics Center, Research School of Physics, Australian National University, Canberra, Australian Capital Territory, Australia. [3]National Mobile Communications Research Laboratory, Frontiers Science Center for Mobile Information Communication and Security, Southeast University, Nanjing, China. [4]Purple Mountain Laboratories, Nanjing, China. [5]Institute of Materials Research and Engineering, A*STAR (Agency for Science Technology, and Research), Singapore, Singapore. [6]Singapore University of Technology and Design, Singapore, Singapore. [7]These authors contributed equally: Sergey S. Kruk, Lei Wang. ✉e-mail: sergey.kruk@outlook.com; wang_lei_seu@seu.edu.cn; yuri.kivshar@anu.edu.au

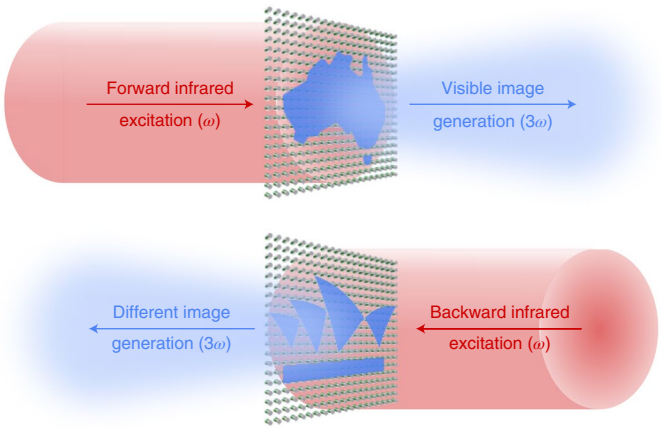

Fig. 1 | Concept of asymmetric parametric generation of images with a nonlinear metasurface. The metasurface generates different and independent images in transmission with two opposite illumination directions. The images are produced at tripled frequency via a nonlinear process of THG.

by the difference in the refractive indices between the two layers. The metasurface is embedded into a homogeneous environment (glass). The geometrical simplicity of our design makes it particularly suitable for standard nanofabrication, such as single-step nanolithography techniques.

Figure 2c,d presents the results of full-wave simulations of our metasurface unit cell. We calculated the total linear extinction cross-section per unit cell, C_{ext}^{total}, of nanoresonators of various radii within the metasurface (details are provided in the Methods). In all the different radii cases, the resonators feature identical total extinction for 'forward' and 'backward' illumination, as required by reciprocity. However, the anisotropy of the resonators' design reveals itself in a decomposition of the extinction into a series of Mie multipoles $C_{ext}^{total} = C_{ext}^{ED} + C_{ext}^{MD} + C_{ext}^{EQ} + C_{ext}^{MQ} \ldots$ (here EQ and MQ stand for electric and magnetic quadrupoles). Figure 2e–h visualizes extinction cross-sections of the two dominant multipoles: the ED and the MD, in forward and backward directions. In addition, Supplementary Fig. 2 includes information about higher-order multipoles. The Mie resonances interact differently in forward and backward directions, which we associate with their magneto-electric coupling. Specifically, forward illumination leads to enhancement of the MD and suppression of the ED, whereas backward illumination leads to the opposite effect of ED enhancement via MD suppression. The modes demonstrate the complex dynamics rendered by their finite spectral width. We notice that the ED and MD Mie resonances tend to have different spectral widths and different Q factors, as is commonly observed in subwavelength dielectric particles[1]. Once higher-order multipoles are considered, the effects of the enhancement/suppression of the resonances are observed between the groups of symmetric and anti-symmetric multipoles dominated by the two dipole modes (details are provided in Supplementary Fig. 2). We provide in the Methods a simplistic analytical insight into the mechanism of enhancement/suppression via magneto-electric coupling of the two dominant modes, ED and MD. We choose a resonator with 215-nm radius that provides the highest contrast in the MD extinction between the forward and backward directions. Figure 2i,j presents the corresponding multipolar composition. At a wavelength of ~1,475 nm, the resonator features an MD maximum for forward illumination and an MD minimum for the backward direction. We note that the effects of MD enhancement/suppression are inherent properties of our bilayer particles, and they are also expected from individual, stand-alone nanoresonators (Supplementary Figs. 1a–d and Supplementary Note 1).

Next we consider the generation of third optical harmonics within the nanoresonators under intense laser illumination. Third-harmonic generation (THG) is a process by which three photons from an excitation beam become 'combined' into a single photon with tripled energy and correspondingly tripled frequency. The THG efficiency here depends on optical modes excited within the resonator, and it is drastically higher for the MD mode than for the ED mode[9]. As such, from the multipolar compositions in Fig. 2i,j, we expect brighter THG in the forward direction (Fig. 3a). Our analysis, up to this point, ignores the optical modes of the resonator at the THG wavelength. However, we expect them to have a smaller effect on the overall THG efficiency compared to the modes at the pump wavelength[9]. It is worth noting that the metasurface consists of subwavelength unit cells at the fundamental frequency, but the unit cell size becomes larger than the wavelength at the third-harmonic frequency.

We carried out full-wave nonlinear calculations of the THG process in our metasurfaces (details are presented in the Methods). Our numerical simulations consider near-field distributions at both the fundamental and THG wavelengths, thus taking into account the optical modes at both frequencies. Figure 3f shows the results of our linear and nonlinear calculations, featuring ~450 times contrast in THG intensity at a wavelength of ~1,475 nm. At the same time, the metasurfaces have identical linear transmission (Fig. 3c). We find it illustrative to compare THG asymmetric generation in our metasurface with THG in a continuous unpatterned bilayer film with otherwise identical parameters (Fig. 3b,e). The THG contrast of such a film does not exceed 1.1. This demonstrates the key role of the interplay of Mie modes in our carefully engineered nanoresonators.

We fabricated the metasurface with electron-beam lithography (details are provided in the Methods and an image of a fabricated metasurface in Fig. 3d, inset). We measured virtually identical linear transmission of the metasurfaces (Fig. 3d) for forward and backward scenarios. We next measured the intensity of the third-harmonic signal in the transmission direction for both scenarios of excitation (Fig. 3g) and observed an ~25 times difference in the intensity of the THG. We note that the contrast in THG is also expected from individual, stand-alone nanoresonators (Supplementary Fig. 1e and Supplementary Note 1).

We proceeded from uniform metasurfaces consisting of identical nanoresonators to non-uniform metasurfaces assembled from a set of dissimilar resonators. Such resonators can generate light via nonlinear parametric processes with different parameters, including different intensity, phase and polarization. We optimized the resonators to produce different levels of THG intensity. With this, we aimed to generate completely different images for the forward and backward excitations. We limited ourselves to images with binary intensity. This requires at least four different types of nanoresonator: an always bright nanoresonator, an always dark nanoresonator, a nanoresonator that is bright for the forward, but dark for the backward directions, and finally a nanoresonator with the opposite functionality that is dark for forward but is bright for backward.

For the sake of nanofabrication simplicity, we required that all the resonators have silicon and silicon nitride layers of the same thickness. To add flexibility to the design approach, we thus introduced two additional geometrical degrees of freedom. We placed the resonators on a glass substrate in air, so the resonators were no longer embedded into an homogeneous environment. The presence of a substrate introduces an additional asymmetry to the system that may also affect the THG process via the magneto-electric coupling[24]. Second, we allowed cylinders with elliptical cross-sections. This extra geometrical parameter (ellipticity of the cross-section) allowed us to equalize the relative brightness levels of the four resonators. To avoid additional polarization effects due to the ellipticity of the resonators, we performed all our studies for the same polarization fixed along one of the axes of the ellipses. Supplementary

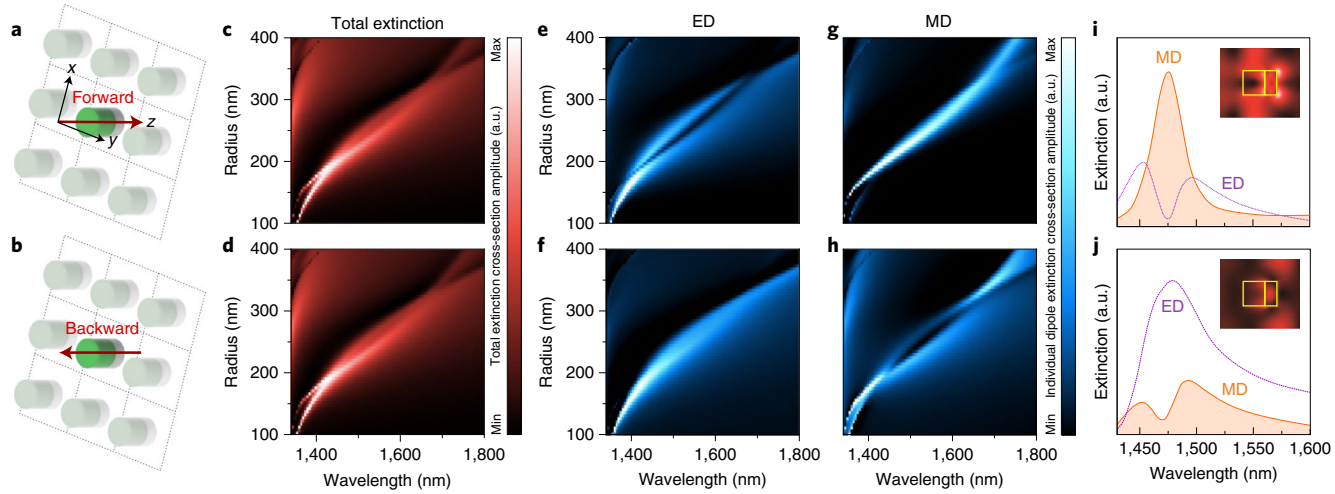

Fig. 2 | Optical properties of a metasurface unit cell. a,**b**, An anisotropic cylindrical nanoresonator consisting of two materials—silicon (grey, 220 nm thick) and silicon nitride (green, 400 nm thick)—embedded into glass. The nanoresonator is placed in a square lattice of identical neighbours with a period of 925 nm, forming a metasurface. Arrows visualize the forward (**a**) and backward (**b**) directions of excitation. **c**,**d**, Linear extinction spectra of the nanoresonators with 100–400-nm radii in the lattice for forward (**c**) and backward (**d**) excitations. **e**–**h**, Contribution of the ED (**e**,**f**) and the MD (**g**,**h**) for forward (**e**,**g**) and backward (**f**,**h**) directions. **i**,**j**, Spectra for the ED (dotted purple curves) and the MD (orange filled curves) of the resonator with 215-nm radius in forward (**i**) and backward (**j**) directions. The insets in **i**,**j** show the near-field distributions of the electric field amplitude for an excitation wavelength of 1,475 nm for forward (**i**) and backward (**j**) directions. Yellow lines in the insets mark the contours of the bilayer nanoresonator.

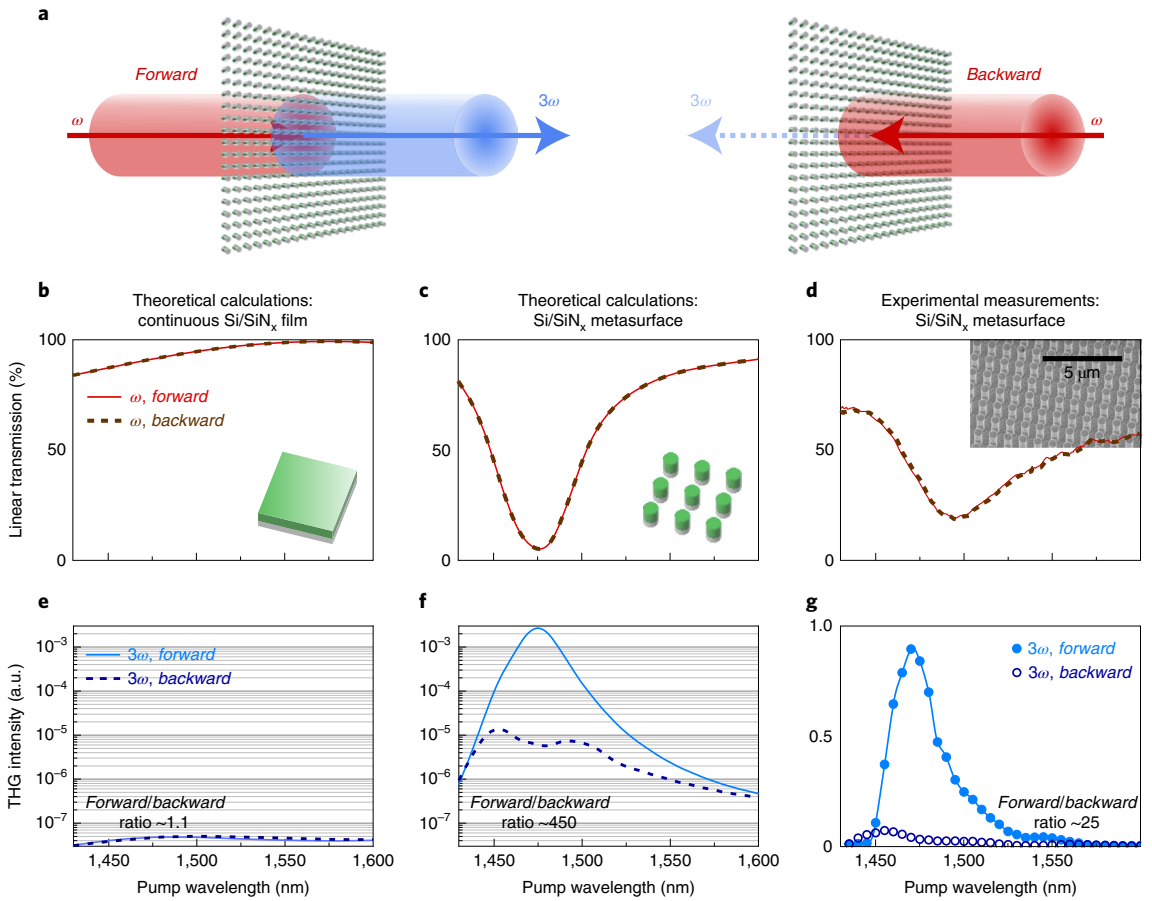

Fig. 3 | Symmetric linear and asymmetric nonlinear spectral response of a uniform metasurface. a, Concept image of two scenarios of THG: for forward and backward directions of excitation. **b**–**f**, Linear transmission (**b**–**d**) and THG (**e**,**f**) for forward and backward excitation. **b**,**e**, Theoretically calculated response of a continuous unpatterned bilayer film (shown in the inset in **b**) of silicon (220 nm) and silicon nitride (400 nm) surrounded by glass. **c**,**f**, Theoretically calculated response of a metasurface (shown in the inset of **c**) consisting of silicon and silicon nitride layers of the same thickness (220 nm and 400 nm correspondingly) embedded into glass, with a cylinder radius of 215 nm and square lattice period of 925 nm. **d**,**g**, Experimental realization of the bilayer metasurface. Inset (**d**): electron microscopy image of the sample, before its embedding into the homogeneous environment.

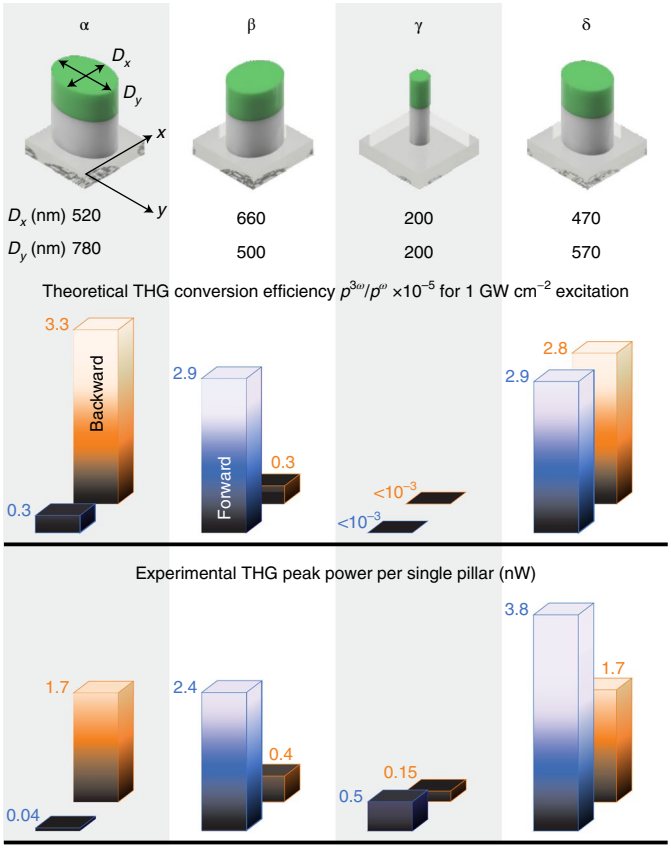

Fig. 4 | Set of resonators with dissimilar asymmetric parametric generation of light. Set of four resonators (α, β, γ, δ) on a glass substrate in air. All the resonators consist of a silicon layer (grey, 480 nm thick) and a silicon nitride layer (green, 360 nm thick). All the resonators are arranged into a square lattice with a period of 900 nm. The elliptical geometries (D_x, D_y) of the resonators in the *x*–*y* plane are listed in the figure. The resonators produce four different combinations of THG responses for forward and backward illumination at a wavelength of 1,475 nm, as specified in the bar charts.

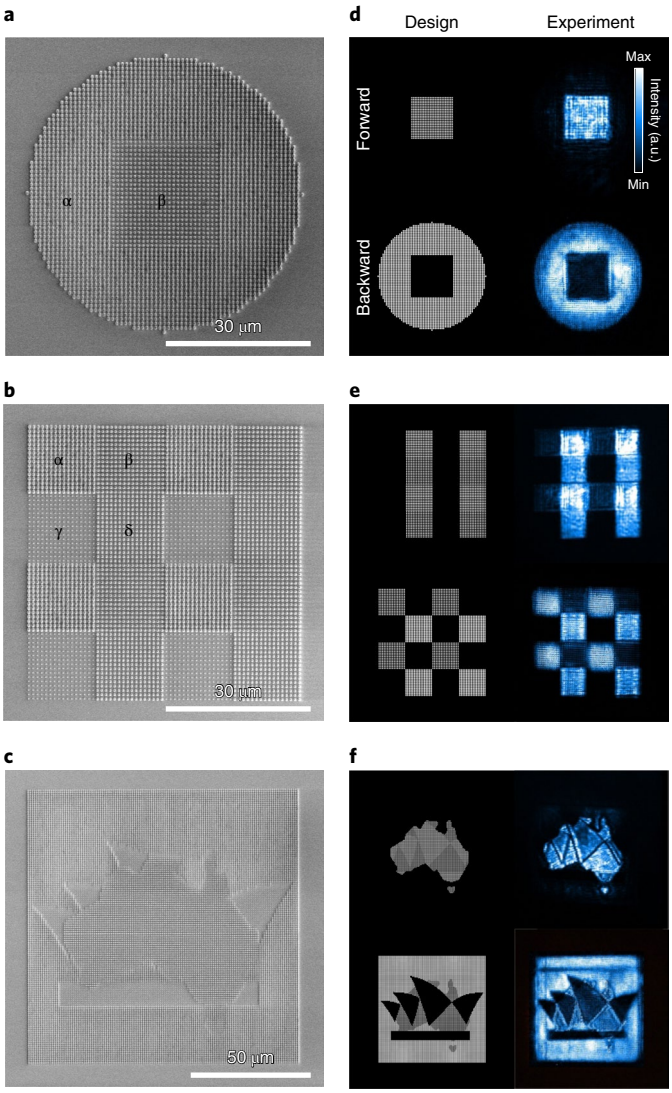

Fig. 5 | Asymmetric parametric generation of images with nonlinear metasurfaces. a–c, Electron microscopy images of three different metasurface layouts assembled from the set of four resonators. **d–f**, Their nonlinear optical response was detected in transmission at the third-harmonic frequency for forward and backward excitation at a wavelength of 1,475 nm. Each of the six experimental images was assigned its own individual minimum and maximum levels of camera counts.

Fig. 3 contains details of numerical optimization of the set of four resonators.

Figure 4 (top) shows the design of the four resonators (marked α, β, γ, δ) and their corresponding theoretically calculated nonlinear optical responses to the forward and backward directions of excitation (middle). The calculated conversion coefficient $P^{3\omega}/(P^{\omega})^3$ reaches 5×10^{-7} W^{-2} for the α pillar and backward illumination. If we assume a power density of 1 GW cm^{-2}, this would give a conversion efficiency $P^{3\omega}/P^{\omega}$ exceeding 3×10^{-5} (for details see Supplementary Note 3 and Supplementary Tables 1–3). The theoretical design features at least nine times THG intensity contrast in the forward direction and at least eight times contrast in the backward direction.

Figure 5a,b presents electron micrographs of three different metasurfaces assembled from the set of four resonators. The metasurface featured in Fig. 5a consists of only two types of nanoresonator (α and β). As shown in Fig. 5d (left side), in the forward direction the metasurface is designed to generate a bright square, whereas in the backward direction it features a bright circle with an embedded dark square. The right side of Fig. 5d shows experimentally observed distributions of third-harmonic signals across the metasurface, as seen in the transmission direction. The experimental observations confirm our theoretical design. Figure 5b,e features a metasurface consisting of all four types of nanoresonator and producing a simple independent pair of images: an image of stripes (forward) and a chessboard pattern (backward). We use the images of the stripes and the chessboard pattern to estimate experimental THG conversion efficiencies of the four dissimilar quadrants in both the forward and backward directions (details are provided in Supplementary Note 4 and Supplementary Tables 4–7). Our estimate suggests that, in experiments, the conversion coefficient for the α pillar and backward illumination is between 1.5×10^{-8} and 7×10^{-8} W^{-2}, which is an order of magnitude lower than the theoretical estimate. We attribute this to fabrication imperfections. The experimental images feature at least 4.5 times contrast in the forward direction and at least four times contrast in the backward direction.

Figure 5c,f feature a metasurface with an encoded pair of arbitrary images: a contour of Australia and a stylistic image of Sydney Opera House. The experimentally observed field distributions resemble closely encoded images. In Fig. 5c,f we note that the edges between the domains of dissimilar resonators can

be observed. These artefacts arise because, near the edges of the domains, the coupling conditions between the near neighbours alter, causing alternation of the THG brightness. In Supplementary Fig. 4 and Supplementary Note 2, we consider one example of an artefact in THG brightness occurring near the edge between the two domains. We demonstrate that a slight alternation of sizes of resonators near the domain wall (by 5 nm in radius or by ~1.5% in the geometrical cross-section) mitigates the artefact. This example suggests that the image imperfections near the edges can be suppressed by means of a slight optimization of the design of the near-edge resonators.

In conclusion, we have demonstrated flexible engineering of asymmetric harmonic generation with metasurfaces. Our metasurfaces are translucent slides, structured at the nanoscale, that generate different images at the third-harmonic wavelength when illuminated from opposite sides. This functionality is enabled by artificially engineered optical interactions beyond the usual electric dipole response, specifically by the optically induced magnetic response and magneto-electric coupling. Our findings pave the way towards novel functionalities of nanoscale optical devices beyond the limits of linear optics. We envision the development of subwavelength resonators and metasurfaces governed by the interplay between magneto-electric coupling and nonlinear light–matter interactions for asymmetric control over multiple parameters of the electromagnetic space, including the spatially modulated amplitude, phase and polarization of optical beams. The functionalities of such resonators can go beyond the parametric generation of light, and the principles revealed in this work may find applications in the asymmetric generation of entangled photon states as well as in asymmetric self-action effects leading to nonreciprocity and optical isolation at the nanoscale.

Online content

Any methods, additional references, Nature Research reporting summaries, source data, extended data, supplementary information, acknowledgements, peer review information; details of author contributions and competing interests; and statements of data and code availability are available at https://doi.org/10.1038/s41566-022-01018-7.

Received: 9 August 2021; Accepted: 28 April 2022;
Published online: 20 June 2022

References

1. Kruk, S. S. & Kivshar, Y. S. Functional meta-optics and nanophotonics governed by Mie resonances. *ACS Photonics* **4**, 2638–2649 (2017).
2. Chen, W. T., Zhu, A. Y. & Capasso, F. Flat optics with dispersion-engineered metasurfaces. *Nat. Rev. Mater.* **5**, 604–620 (2020).
3. Kamali, S. M., Arbabi, E., Arbabi, A. & Faraon, A. A review of dielectric optical metasurfaces for wavefront control. *Nanophotonics* **7**, 1041–1068 (2018).
4. Gallo, K., Assanto, G., Parameswaran, K. R. & Fejer, M. M. All-optical diode in a periodically poled lithium niobate waveguide. *Appl. Phys. Lett.* **79**, 314–316 (2001).
5. Lepri, S. & Casati, G. Asymmetric wave propagation in nonlinear systems. *Phys. Rev. Lett.* **106**, 164101 (2011).
6. Biancalana, F. All-optical diode action with quasiperiodic photonic crystals. *J. Appl. Phys.* **104**, 93113 (2008).
7. Li, G., Zhang, S. & Zentgraf, T. Nonlinear photonic metasurfaces. *Nat. Rev. Mater.* **2**, 17010 (2017).
8. Krasnok, A., Tymchenko, M. & Alù, A. Nonlinear metasurfaces: a paradigm shift in nonlinear optics. *Mater. Today* **21**, 8–21 (2017).
9. Zubyuk, V., Carletti, L., Shcherbakov, M. & Kruk, S. Resonant dielectric metasurfaces in strong optical fields. *APL Mater.* **9**, 060701 (2021).
10. Schlickriede, C. et al. Imaging through nonlinear metalens using second harmonic generation. *Adv. Opt. Mater.* **30**, 1703843 (2018).
11. D'Aguanno, G. et al. Nonlinear topological transitions over a metasurface. *Phys. Rev. B* **100**, 214310 (2019).
12. Huang, Z., Baron, A., Larouche, S., Argyropoulos, C. & Smith, D. R. Optical bistability with film-coupled metasurfaces. *Opt. Lett.* **40**, 5638–5641 (2015).
13. Divitt, S., Zhu, W., Zhang, C., Lezec, H. J. & Agrawal, A. Ultrafast optical pulse shaping using dielectric metasurfaces. *Science* **364**, 890–894 (2019).
14. Koshelev, K. et al. Subwavelength dielectric resonators for nonlinear nanophotonics. *Science* **367**, 288–292 (2020).
15. Bender, N. et al. Observation of asymmetric transport in structures with active nonlinearities. *Phys. Rev. Lett.* **110**, 234101 (2013).
16. Shitrit, N. et al. Asymmetric free-space light transport at nonlinear metasurfaces. *Phys. Rev. Lett.* **121**, 046101 (2018).
17. Mahmoud, A. M., Davoyan, A. R. & Engheta, N. All-passive nonreciprocal metastructure. *Nat. Commun.* **6**, 8359 (2015).
18. Poutrina, E. & Urbas, A. Multipolar interference for non-reciprocal nonlinear generation. *Sci. Rep.* **6**, 25113 (2016).
19. Kim, K. H. Asymmetric second-harmonic generation with high efficiency from a non-chiral hybrid bilayer complementary metasurface. *Plasmonics* **16**, 77–82 (2021).
20. Lawrence, M., Barton, D. R. & Dionne, J. A. Nonreciprocal flat optics with silicon metasurfaces. *Nano Lett.* **18**, 1104–1109 (2018).
21. Jin, B. & Argyropoulos, C. Self-induced passive nonreciprocal transmission by nonlinear bifacial dielectric metasurfaces. *Phys. Rev. Appl.* **13**, 054056 (2020).
22. Cheng, L. et al. Superscattering, superabsorption and nonreciprocity in nonlinear antennas. *ACS Photonics* **8**, 585–591 (2021).
23. Asadchy, V. S., Díaz-Rubio, A. & Tretyakov, S. A. Bianisotropic metasurfaces: physics and applications. *Nanophotonics* **7**, 1069–1094 (2018).
24. Kruk, S. et al. Nonlinear light generation in topological nanostructures. *Nat. Nanotechnol.* **14**, 126–130 (2019).
25. Zhao, Y., Belkin, M. A. & Alù, A. Twisted optical metamaterials for planarized ultrathin broadband circular polarizers. *Nat. Commun.* **3**, 870 (2012).
26. Svirko, Y., Zheludev, N. & Osipov, M. Layered chiral metallic microstructures with inductive coupling. *Appl. Phys. Lett.* **78**, 498–500 (2001).
27. Menzel, C. et al. Asymmetric transmission of linearly polarized light at optical metamaterials. *Phys. Rev. Lett.* **104**, 253902 (2010).
28. Pfeiffer, C., Zhang, C., Ray, V., Guo, L. J. & Grbic, A. High performance bianisotropic metasurfaces: asymmetric transmission of light. *Phys. Rev. Lett.* **113**, 023902 (2014).
29. Ra'Di, Y., Asadchy, V. S. & Tretyakov, S. A. Tailoring reflections from thin composite metamirrors. *IEEE Trans. Antennas Propag.* **62**, 3749–3760 (2014).
30. Albooyeh, M., Alaee, R., Rockstuhl, C. & Simovski, C. Revisiting substrate-induced bianisotropy in metasurfaces. *Phys. Rev. B* **91**, 195304 (2015).
31. Zhirihin, D. V. et al. Photonic spin Hall effect mediated by bianisotropy. *Opt. Lett.* **44**, 1694–1697 (2019).
32. Gorlach, A. A., Zhirihin, D. V., Slobozhanyuk, A. P., Khanikaev, A. B. & Gorlach, M. A. Photonic Jackiw-Rebbi states in all-dielectric structures controlled by bianisotropy. *Phys. Rev. B* **99**, 205122 (2019).
33. Khanikaev, A. B. et al. Photonic topological insulators. *Nat. Mater.* **12**, 233–239 (2012).

Methods

Numerical calculations. We simulated the generation of the third-harmonic signal using the finite-element-method solver in COMSOL Multiphysics in the frequency domain. All our simulations model the metasurfaces as periodic structures with identical nanoresonators with Floquet boundary conditions. Our nonlinear calculations are based on undepleted pump approximation and are performed in two stages. For the first stage, we calculate linear light–matter interactions and retrieve the electromagnetic field distributions at the fundamental frequency in the nanoresonator. The pump is a plane wave with a power density of 1 GW cm^{-2}. We then deduce the current density J_{THG} of the THG within the silicon particle by multiplying the third-order nonlinear susceptibility tensor $\chi^{(3)}$ and the linear field distributions. For the second stage, we employ J_{THG} as a source of external current density for the simulation and retrieve the nonlinear optic field distribution at the THG frequency. We approximate the $\chi^{(3)}$ tensor for amorphous silicon to a non-dispersive scalar value of 2.45×10^{-19} m^2 V^{-2}. For the case of a metasurface composed of dissimilar nanoresonators, we simplify the model by assuming that the coupling between non-identical nanoresonators is roughly the same as that with identical ones.

To find an optimal design for the nanoresonators, we optimized the parameter space of five geometrical dimensions: the thickness of each material layer (h_1, h_2), the long and short axes of the ellipses (D_1, D_2) and the square unit cell size (P) (this is reduced to four-parameter space when $D_1 = D_2$ for an homogeneous metasurface).

To enhance the computing speed, we implemented multigoal global genetic optimization algorithms to guide the COMSOL calculations. This method analyses the calculated datasets in each generation as goal functions with the corresponding selecting criteria depending on the desirable characteristics. For example, selecting criteria for the metasurface in Fig. 2 are (s1) and (s2). For atoms in Fig. 4 they are as follows: α, (s1) and (s3); β, (s1) and (s4); γ, (s6); δ, (s1) and (s5), respectively. The (s1) criterion is the third-harmonic conversion efficiency in the desirable illumination direction, (s2) is the third-harmonic intensity contrast between the forward and backward illumination regimes, (s3) is THG predominantly in the direction of the incident wave for the backward case of illumination, (s4) is THG for forward cases of illumination, (s5) is THG for both cases of illumination and (s6) is low THG efficiency for both illuminations. In the algorithm, the geometrical parameters set for the nanoresonators are treated as genomes, which evolve to reach optimization. Supplementary Fig. 3 illustrates the results of the numerical investigation.

Analytical description of the magneto-electric coupling. To yield a simplistic analytical insight, we approximated the optical response of our nanoresonators down to only ED and MD modes, leaving weaker higher-order multipoles without consideration. We assumed that the metasurface response can be grasped by effective polarizability tensors $\overline{\overline{\alpha}}_{\mathrm{ee}}$ (electric), $\overline{\overline{\alpha}}_{\mathrm{mm}}$ (magnetic) and $\overline{\overline{\alpha}}_{\mathrm{me}}$ (magneto-electric). Without a lack of generality, we will focus on x-polarized light beams propagating in the $\pm z$ directions. The response will thus be governed by $\alpha_{\mathrm{ee}}^{xx}$, $\alpha_{\mathrm{mm}}^{yy}$, $\alpha_{\mathrm{me}}^{xy}$ and $\alpha_{\mathrm{me}}^{yx}$ components of the tensors. We further assumed that the metasurface obeys optical reciprocity in the linear regime. This further reduces the number of polarizability terms: $\alpha_{\mathrm{me}}^{xy} = -\alpha_{\mathrm{me}}^{yx}$. Under this condition, the excitation of the ED and MD modes can be written as

$$\begin{aligned} p_x &= \alpha_{\mathrm{ee}}^{xx} E_x \pm \alpha_{\mathrm{me}}^{xy} H_y \\ m_y &= \pm\alpha_{\mathrm{mm}}^{yy} H_y - \alpha_{\mathrm{me}}^{xy} E_x \end{aligned} \tag{1}$$

where E_x and H_y are local fields at the position of a nanoresonator. The '±' sign in front of the H_y term accounts for the cases of forward and backward illumination. From equation (1) we can see that the MD mode is enhanced for the forward illumination and is suppressed for the backward illumination by magneto-electric coupling. The enhancement or suppression of the ED mode is opposite that of the MD mode. Notably, the strength of magneto-electric coupling described by $\alpha_{\mathrm{me}}^{xy}$ conceptually may take arbitrarily large values, reaching or even exceeding the strengths of the electric and magnetic responses described via the $\alpha_{\mathrm{ee}}^{xx}$ and $\alpha_{\mathrm{mm}}^{yy}$ components[34,35]. Interestingly, a balance between the polarizability tensors may lead to complete suppression of a given dipole mode for a given direction of excitation:

$$\begin{aligned} &p_x = 0 \text{ for } Z_0\alpha_{\mathrm{ee}}^{xx} = \alpha_{\mathrm{me}}^{xy} \text{ and forward } \left(+H_y\right) \text{ propagation} \\ &m_y = 0 \text{ for } \tfrac{1}{Z_0}\alpha_{\mathrm{mm}}^{yy} = \alpha_{\mathrm{me}}^{xy} \text{ and backward } \left(-H_y\right) \text{ propagation} \end{aligned} \tag{2}$$

Here, Z_0 is the impedance of the homogeneous environment.

Calculation of extinction and multipole coefficients. We derive the total extinction cross-section per unit cell by evaluating the energy flux and total loss within the unit cell through numerically solved near-field information. Total extinction is the sum of total scattering and absorption $C_{\mathrm{ext}}^{\mathrm{total}} = C_{\mathrm{scatter}}^{\mathrm{total}} + C_{\mathrm{absorb}}^{\mathrm{total}}$. The total scattering cross-section per unit cell $C_{\mathrm{scatter}}^{\mathrm{total}}$ is equal to Q_{sca}/I_0, and the scattered energy flux Q_{sca} can be computed via the surface integral of the Poynting vector of the scattered field over the open boundaries of the unit cell, and I_0 is the intensity of the incident light wave. $C_{\mathrm{absorb}}^{\mathrm{total}}$ is equal to the volume integral of the loss Q_{h} in the domain of the nanoresonator, which is usually neglectable for silicon material.

The electric and magnetic multipole coefficients can be derived from the numerically solved scattering current density $J(r)$ by solving partial differential equations using the multipole decomposition methods detailed in ref. [36]. The multipole terms for the averaged extinction per unit cell, $C_{\mathrm{ext}}^{\mathrm{ED}}$, $C_{\mathrm{ext}}^{\mathrm{MD}}$, $C_{\mathrm{ext}}^{\mathrm{EQ}}$, $C_{\mathrm{ext}}^{\mathrm{MQ}}\ldots$, can therefore be calculated using equation (3) with $l = 1, 2, 3$ as dipole, quadrupole and octupole terms:

$$\begin{aligned} C_{\mathrm{ext}}^{\mathrm{E},\,l} &= -\tfrac{\pi}{k^2}\sum_{m=-1,\,+1}(2l+1)\mathrm{Re}[m a_{\mathrm{E}}(l,\,m)] \\ C_{\mathrm{ext}}^{\mathrm{M},\,l} &= -\tfrac{\pi}{k^2}\sum_{m=-1,\,+1}(2l+1)\mathrm{Re}[a_{\mathrm{M}}(l,\,m)] \end{aligned} \tag{3}$$

In this work, the multipolar analysis was performed using COMSOL. Some of the technical details on multipole analysis in COMSOL can be found in ref. [37].

Nanofabrication. The metasurfaces were fabricated on a glass substrate using a multi-step process that begins with consecutive deposition of thin films of amorphous silicon and silicon nitride of desired thicknesses by plasma-enhanced chemical vapour deposition. For the homogeneous metasurface (Fig. 3), a silicon nitride thin film is deposited first, followed by deposition of an amorphous silicon film. For the inhomogeneous metasurface (Fig. 4), the silicon nitride film is deposited after the amorphous silicon film. A polymethyl-methacrylate resist layer is spin-coated onto the bilayer films and baked on a hot plate at 170 °C for 2 min to remove the solvent. The desired patterns are then transferred using standard electron-beam lithography and subsequent development in 1:3 methyl isobutyl ketone:isopropyl alcohol (IPA) solution. During the electron-beam writing process, multiple sets of samples are patterned with both positive and negative size biases to accommodate possible size deviations during the fabrication. Next, a 20-nm-thick chromium mask is deposited by electron-beam evaporation. After a liftoff process in hot acetone, the patterns are transferred from polymethyl-methacrylate to the chromium. Finally, the structures are transferred onto the bilayer material using inductively coupled plasma reactive ion etching and subsequent removal of the chromium mask by a commercially purchased chromium-etch solution. Note that each material layer within the bilayer film is etched by a recipe optimized to that specific material. Electron microscopy images of the resulting sample were obtained using a scanning electron microscope. The homogeneous metasurfaces were further embedded into a droplet of optical oil with a refractive index like that of the glass substrate, then covered by a glass slide identical to the substrate slide.

Optical measurements. For linear spectral measurements, a tungsten halogen light bulb was used as the light source. In experiments for nonlinear optical measurements, a pulsed laser system was used as the light source. This consisted of a Femtolux Ekspla laser (1,030-nm wavelength) and a Hotlight Systems MIROPA optical parametric amplifier (wavelength tunability range of 1,350–1,750 nm). Optical pulses with 2-ps duration, a 5-MHz repetition rate and linear horizontal polarization were used. The average output power of the laser system was 500 mW at a wavelength of 1,450 nm, decreasing for other wavelengths. The power was monitored by an Ophir IR power meter. The collimated laser beam was narrowed by achromatic doublet lenses (Thorlabs) to illuminate an area of ~200 ± 25 μm, which is about twice as large as the metasurface in Fig. 5c and approximately four times larger than the metasurfaces in Fig. 5a,b. Both the infrared excitation and the visible light generated a third-harmonic signal that was captured by an objective lens (Mitutoyo Plan Apo NIR HR ×100 NA 0.7) with an achromatic performance across the 400–1,800-nm spectral range. The infrared spectra were measured with a NIR-Quest spectrometer (Ocean Optics), and the visible spectra were monitored by a QE Pro spectrometer (Ocean Optics). The metasurface images in the infrared were recorded on a Xenics Bobcat 320 camera paired with an infinity-corrected $f = 150$ mm infrared achromatic doublet lens (Thorlabs). The metasurface images in the visible range were recorded on a Trius-SX694 Starlight Xpress camera paired with an infinity-corrected $f = 150$ mm visible achromatic doublet lens (Thorlabs). For measurements at the third-harmonic frequency, the excitation wavelength was filtered by FGB900 colour glass. The forward and backward illumination directions were recorded by flipping the sample around the vertical axis. The parameters of the excitation laser were kept the same for the forward and backward experiments. The experimental backward images were correspondingly mirrored along the vertical axis in post-processing. An aperture diaphragm was added in the back focal plane of the imaging objective to ensure the collection of only the forward-propagating signal. The resolution of the forward images was reduced in comparison to the backward images by aberrations introduced by the substrate.

Data availability

All data in this study are available within the paper and the Supplementary Information. Additional information will be provided by S.K. and L.W. on reasonable request.

Code availability

The code used for modelling the data is available for download at https://pan.seu.edu.cn:443/link/4A3683E9DA843E10D06FFBA5B43DCDFD. Additional information will be provided by L.W. on reasonable request.

References

34. Albooyeh, M. et al. Purely bianisotropic scatterers. *Phys. Rev. B* **94**, 245428 (2016).
35. Ra'Di, Y. & Tretyakov, S. A. Balanced and optimal bianisotropic particles: maximizing power extracted from electromagnetic fields. *New J. Phys.* **15**, 053008 (2013).
36. Grahn, P., Shevchenko, A. & Kaivola, M. Electromagnetic multipole theory for optical nanomaterials. *New J. Phys.* **14**, 093033 (2012).
37. Multipole Analysis of Electromagnetic Scattering (COMSOL. 2015); https://cn.comsol.com/model/download/588151/

Acknowledgements

We thank V. Asadchy, A. Alu, C. Caloz, A. Poddubny, D. Smirnova, K. Simovski, I. Shadrivov and S. Tretyakov for numerous stimulating discussions. We acknowledge the use of the nanofabrication facility at Paderborn University and acknowledge the Australian National Fabrication Facility, ACT Node, for access to the electron microscope. S.S.K. acknowledges support from the Alexander von Humboldt Foundation, the Australian Research Council (DE210100679) and the EU Horizon 2020 research and innovation programme (grant no. 896735). Z.D. acknowledges help from F. Tjiptoharsono with the fabrication etching recipe. T.Z. acknowledges funding by the European Research Council (ERC) under the European Union's Horizon 2020 research and innovation programme (grant agreement no. 724306) and the Deutsche Forschungsgemeinschaft (DFG, German Research Foundation; TRR142, no. 231447078, project B09). L.W. acknowledges support from the National Key R&D Program of China (2020YFB1806603), the National Natural Science Foundation of China (grant no. 62101127), the Natural Science Foundation of Jiangsu Province of China (BK20200393), SC project of Jiangsu Province (JSSCBS20210116) and the Fundamental Research Funds for the Central Universities (2242022R10025). Y.K. acknowledges support from the Strategic Fund of the Australian National University, the Australian Research Council (grant no. DP210101292) and the US Army International Office (grant no. FA520921P0034).

Author contributions

S.S.K. and L.W. conceived the idea. L.W. performed theoretical calculations. B.S., Z.D. and S.S.K. fabricated the samples. S.S.K. and L.W. performed experimental measurements. J.Y., T.Z. and Y.K. contributed to data analysis and to supervision of the project. S.S.K. wrote the first version of the manuscript. All co-authors contributed extensively to writing and to revisions of the manuscript.

Competing interests

The authors declare no competing interests.

Additional information

Supplementary information The online version contains supplementary material available at https://doi.org/10.1038/s41566-022-01018-7.

Correspondence and requests for materials should be addressed to Sergey S. Kruk, Lei Wang or Yuri Kivshar.

Peer review information *Nature Photonics* thanks Christos Argyropoulos, Yuanmu Yang and the other, anonymous, reviewer(s) for their contribution to the peer review of this work.